Award Number:

W81XWH-11-1-0197

TITLE:

Eye TVR: Eye Trauma & Visual Restoration Team

PRINCIPAL INVESTIGATOR:

James Weiland, PhD

CONTRACTING ORGANIZATION:

UNIVERSITY OF SOUTHERN CALIFORNIA
LOS ANGELES, CA 90089-9235

REPORT DATE:

March 2013

TYPE OF REPORT:

Final

PREPARED FOR: U.S. Army Medical Research and Materiel Command
                         Fort Detrick, Maryland 21702-5012

DISTRIBUTION STATEMENT:

 Approved for public release; distribution unlimited

REPORT DOCUMENTATION PAGE

1. REPORT DATE *(DD-MM-YYYY)*	2. REPORT TYPE	3. DATES COVERED *(From - To)*
Tå&@201H	Final	18 Feb¦˘æˆ 2011- 17 Feb¦˘æˆ 2013

4. TITLE AND SUBTITLE	5a. CONTRACT NUMBER
Eye TVR: Eye Trauma & Visual Restoration Team	
	5b. GRANT NUMBER
	ÙÎFVÙÒËFFËFˀFÏÍ
	5c. PROGRAM ELEMENT NUMBER

6. AUTHOR(S)	5d. PROJECT NUMBER
James Weiland, Shuliang Jiao, Victor Pikov, and Douglas McCreery.	
	5e. TASK NUMBER
	5f. WORK UNIT NUMBER

7. PERFORMING ORGANIZATION NAME(S) AND ADDRESS(ES)	8. PERFORMING ORGANIZATION REPORT NUMBER
UNIVERSITY OF SOUTHERN CALIFORNIA LOS ANGELES, CA 90089-9235	

9. SPONSORING / MONITORING AGENCY NAME(S) AND ADDRESS(ES)	10. SPONSOR/MONITOR'S ACRONYM(S)
U.S. Army Medical Research and Materiel Command Fort Detrick, Maryland 21702-5012	
	11. SPONSOR/MONITOR'S REPORT NUMBER(S)

12. DISTRIBUTION / AVAILABILITY STATEMENT
Approved for public release; distribution unlimited

13. SUPPLEMENTARY NOTES

14. ABSTRACT
The EyeTVR team conducts applied research aimed at saving and restoring sight to the war fighter who suffers traumatic eye injury. The larger goal is also to help veterans and their family members who suffer from eye injury, eye infection, and inherited or age-related eye disease. The research achieved the following aims: (1) developed a dual-band OCT system for investigating the spectral contrast for the diagnosis of early damage to the retinal nerve fiber layer; (2) investigated millimeter wave stimulation for functional retinal diagnostics; (3) conducted experiments on active sensor for mobility aid to blind; (4) developed an advanced neural interface system for a cortical visual prosthesis.

15. SUBJECT TERMS
Optical coherence tomography, image segmentation, image registration

16. SECURITY CLASSIFICATION OF: U			17. LIMITATION OF ABSTRACT	18. NUMBER OF PAGES	19a. NAME OF RESPONSIBLE PERSON USAMRMC
a. REPORT U	b. ABSTRACT U	c. THIS PAGE U	UU	25	19b. TELEPHONE NUMBER *(include area code)*

TABLE OF CONTENTS

INTRODUCTION

A March 9, 2008 article in the *San Francisco Chronicle* ("*New treatments for traumatic eye injuries*") highlighted the incidence of eye injuries in the Iraq war (more than double those in World War II). Eye wounds have become among the most common - and devastating - form of battlefield injury, with an estimated 10 to 13% of wounded Iraq veterans sustaining direct, penetrating eye damage. Serious eye wounds have accumulated at almost twice the rate as wounds requiring amputations. In a recent article in the *Army Times*, it was estimated that 1,400 troops have vision problems caused by combat injuries. According to the Blinded Veterans Association, 75% of service members with traumatic brain injuries also have vision problems including double vision, lack of peripheral vision, color blindness and total blindness.

The EyeTVR team conducts applied research aimed at saving and restoring sight to the war fighter who suffers traumatic eye injury. The larger goal is also to help veterans and their family members who suffer from eye injury, eye infection, and inherited or age-related eye disease. The research projects are in the following two groups:

1. **Functional Imaging** — to develop innovative methods to visualize retinal structure to determine whether cells of the retina and optic nerve are functioning properly.
   Tasks: a. Spectral contrast for the diagnosis of early damage to the retinal nerve fiber layer.
   b. Millimeter wave stimulation for functional retinal diagnostics.
2. **Visual Prosthesis and Biomaterials** — to develop materials to promote eye wound healing and attachment of devices to the retina and the visual centers of the brain, enabling the functional placement of visual prosthesis or drug delivery systems.
   Tasks: a. Active sensor for mobility aid to blind.
   b. An advanced neural interface system for a cortical visual prosthesis.

BODY

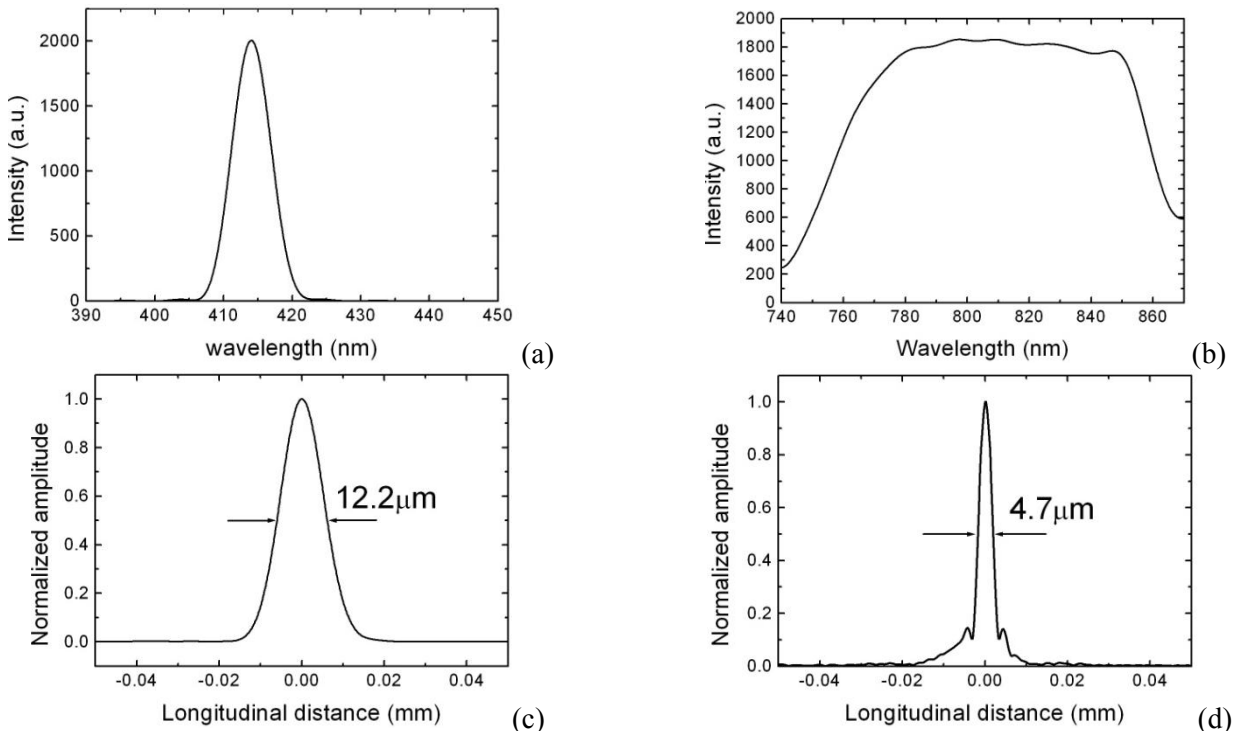## Task 1a: Spectral contrast for the diagnosis of early damage to the retinal nerve fiber layer

Fig. 1 Calibrated OCT parameters in the VIS and NIR spectra. (a): the measured VIS spectrum; (b): the measured NIR spectrum; (c) the measured point spread function (PSF) of the VIS OCT; (d) the measured PSF of the NIR OCT.

We worked on building the OCT systems in the visible (VIS) and near infrared (NIR) spectra. The light source for the two OCT systems is a broadband Ti:Sapphire ultra-fast laser centered at 800 nm (Micra-5, Coherence, USA). We use a BBO crystal (CASTECH Inc, China) to double the light frequency. To increase the bandwidth of the frequency doubled light, the fundamental light is focused onto the crystal by an objective lens with a focal length of 14 mm. We used a long-pass filter (FEL0600, Thorlabs, USA) to separate the frequency-doubled light and the residue fundamental light. After the long-ass filter the separated VIS and NIR light beams are coupled into the source arms of their corresponding fiber-based Michelson interferometers. The spectrum of the VIS light is shown in Fig. 1a, which has a center wavelength of 415 nm and a FWHM bandwidth of about 10 nm. The measured point spread function (PSF) of the VIS OCT is shown in Fig. 1c. The calibrated depth resolution is 12.2 µm in air. The spectrum of the NIR light is shown in Fig. 1b, which has a center wavelength of 800 nm and a FWHM bandwidth of about 100 nm. The measured PSF of the NIR OCT is shown in Fig. 1d. The calibrated depth resolution is 4.7 µm in air.

We then integrated the two OCT systems on a slit lamp. After the animal protocol was approved by ACURO we conducted animal experiments. The system was applied to imaging the normal rat retina *in vivo*. The animals (Sprague Dawley rats, body weight: 600~750 g, Charles Rivers) were anesthetized by intraperitoneal injection of a cocktail containing ketamine (54 mg/kg body weight) and xylazine (6 mg/kg body weight). In the meantime, the pupils were dilated with 10% phenylephrine solution. Drops of artificial tears were applied to the eyes every two minutes to prevent dehydration of the cornea and cataract formation. After anesthetization, the animals were restrained in a mounting tube, which was fixed on a five-axis platform. Raster scans with the fast axis along the horizontal direction were performed. All experiments were performed in compliance with the guidelines of the University of Southern California's Institutional Animal Care and Use Committee.

In the experiment, we collected the NIR and VIS-OCT images sequentially. The initial alignment including finding the area of interest was done with the NIR OCT. After the acquisition of the NIR OCT image we mechanically switched the VIS OCT into position and acquired the VIS OCT images. In our current study the laser energy after the objective lens was measured to be 450 µW for the visible and 750 µW for the NIR light, which are both below the ANSI safety limits for eye imaging. Since the OCT images of the two different bands were not acquired simultaneously they are not completely registered due to movement of the animal during the switching process. The advantage of using the NIR-OCT for alignment is to reduce the retinal exposure to the visible light. The higher axial resolution and greater imaging depth of the NIR-OCT also aided the alignment.
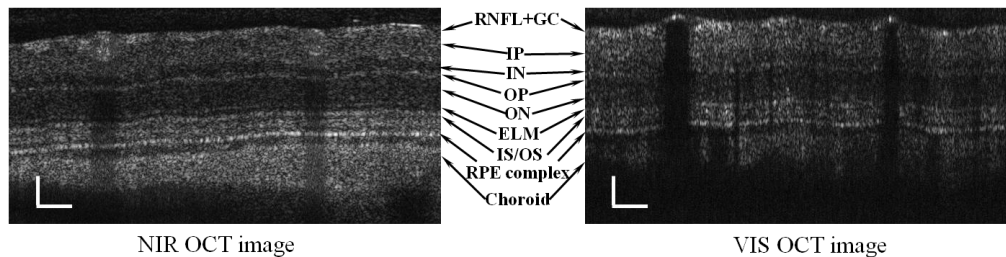

RNFL+GC
IP
IN
OP
ON
ELM
IS/OS
RPE complex
Choroid

NIR OCT image   VIS OCT image

Fig. 2 Sample images of a rat retina acquired with the NIR OCT and VIS OCT. Images consist of 2048 A-lines. Bar: 100 µm.

Figure 2 shows one pair of the acquired NIR and VIS OCT images. The images consist of 2048 A-scans and cover a length of about 1.3 mm across the retina. The differences between the NIR and VIS OCT images are significant. As expected the blood vessels blocked the VIS probing light completely with only reflections from their front boundaries, while the NIR-OCT still revealed some features beneath the vessels. This difference comes from the significant difference of the absorption coefficients of hemoglobin at the two bands: at 415 nm $\mu_a = 2801.52$ (cm^{-1}) for oxy-hemoglobin (HbO$_2$) and $\mu_a = 1891.79$ (cm^{-1}) for deoxy-hemoglobin (Hb); at 808 nm $\mu_a = 4.58$ (cm^{-1}) for HbO2 and $\mu_a = 3.88$ (cm^{-1}) for Hb.

Task 1b: Millimeter wave stimulation for functional retinal diagnostics

The overall goal of this project is to develop a technology for non-invasive neuromodulation of retinal activity. Our approach is to measure the neuronal activity in vivo while the eye is exposed to the focused beam of millimeter waves (MMW). A number of key tasks were completed.

1. Development of real-time user-friendly interface for measuring evoked retinal responses

The software for optical/MMW stimulation and multichannel neural data acquisition was developed using the Visual Basic 6.0 (Microsoft Corp.) and Measurement Studio ActiveX components (National Instruments Inc.). Fig. 3 shows a sample screenshot of the graphical user interface:
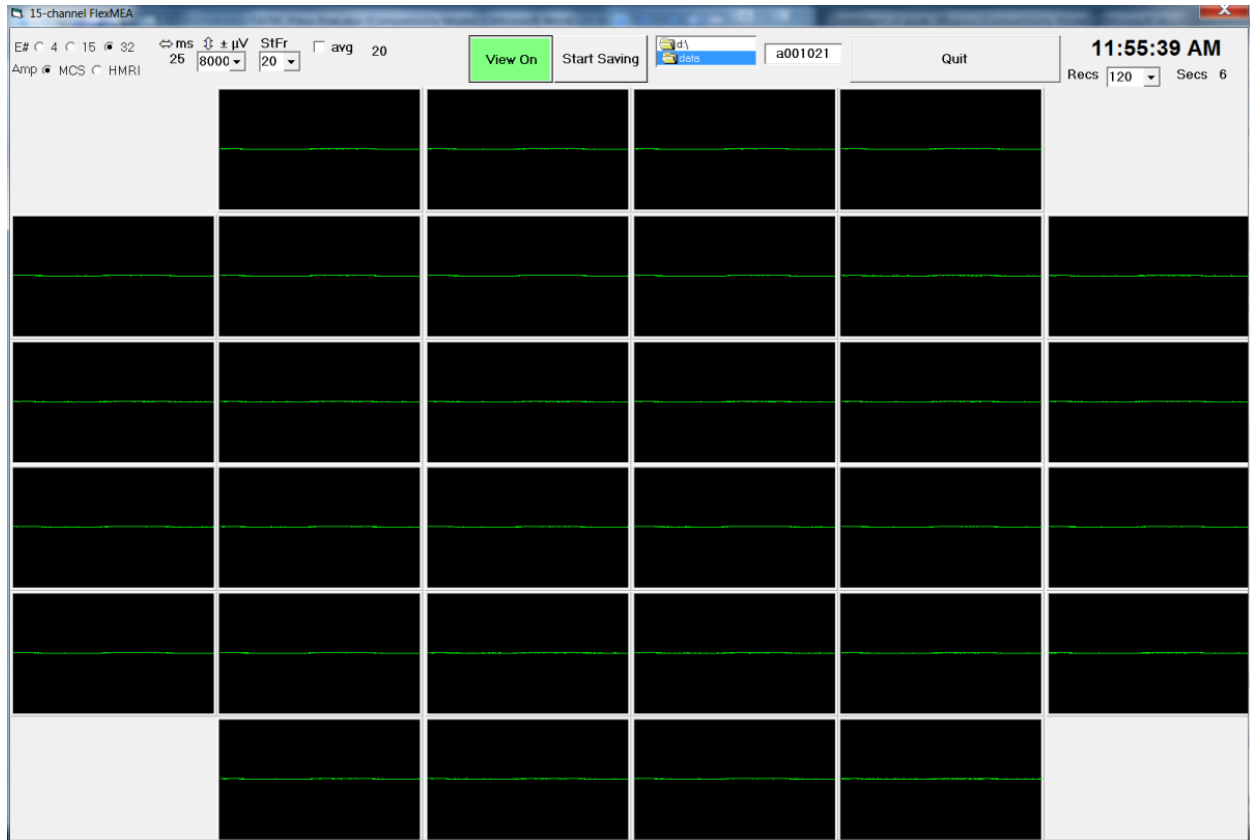

Fig. 3. Graphical user interface for neural data acqisition.

The interface accommodates multiple electrode array types, ranging from 4 to 32 channels. The data acquisition is hardware-synchronized with the generation of the TTL pulse that can be used to trigger an optical or MMW stimulation. The second program was created for off-line viewing of the recorded data and its export to Matlab for further analysis.

2. Measurement of retinal responses to calibrated optical flash stimuli with 10% or less within-animal within-session error

Our original goal was to use the electroretinography (ERG), however we quickly realized that we would like to get the information about the spatial distribution of the stimulus in the retina, which is not available in the single-channel ERG. We have examined three techniques potentially suitable for recording spatially-resolved retinal responses:

    a. epiretinal recordings,

    b. subretinal recordings,

    c. visual cortex recordings.

To enable such recordings, we have evaluated three types of flexible multi-electrode arrays (MEAs): 4-channel with 200-um diameter sites, 15-channel with 400-um diameter sites, and 15-channel with 50-um

6

diameter sites. These MEAs feature different geometries and flexibility. Fig. 4 shows the sample insertions of the 15-channel MEA into the epiretinal and subretinal space in the rat.
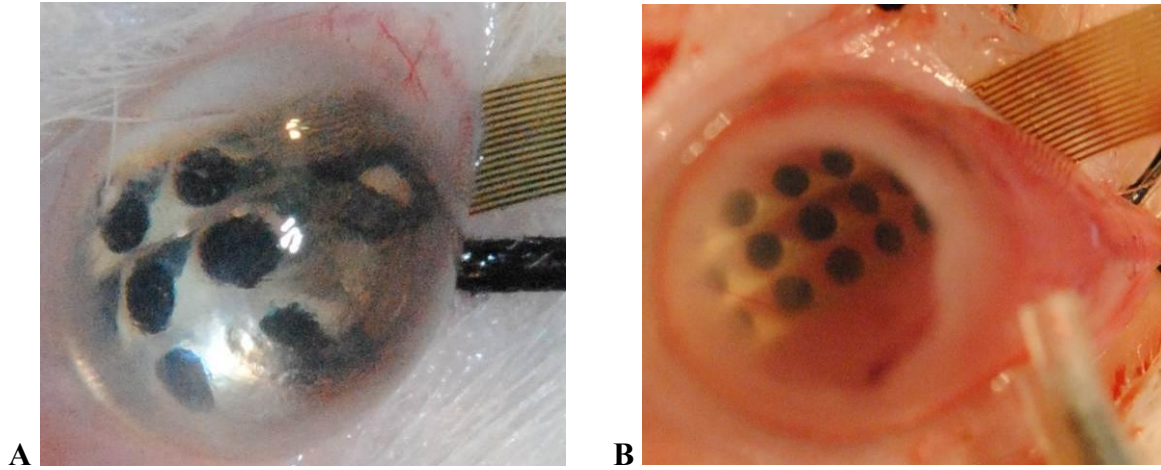

Fig. 4. Photographs of the epiretinal (A) and subretinal (B) placement of the flexible MEA.

Disappointingly, neural recordings could not be obtained from epiretinal and subretinal spaces. We speculate that our inability to record is caused by insufficient proximity of the MEA to the retina on the epiretinal side and by a lack of firing neuronal cells on the subretinal side (photoreceptors and bipolar cells do not fire many action potentials). We then explored whether the flexible MEAs can be used for subdural recordings from the V1 cortical region. Considering the 1-mm distance of the MEA to the layer 3 of the cortex, it is practically impossible to record the multi-unit neuronal activity. Instead, we decided to record the evoked local field potentials (eLFPs). Initial calibration of our software and hardware setup was successfully done by electrically stimulating the hindlimb muscle while recording in the contralateral M1 motor cortex with the MEA.

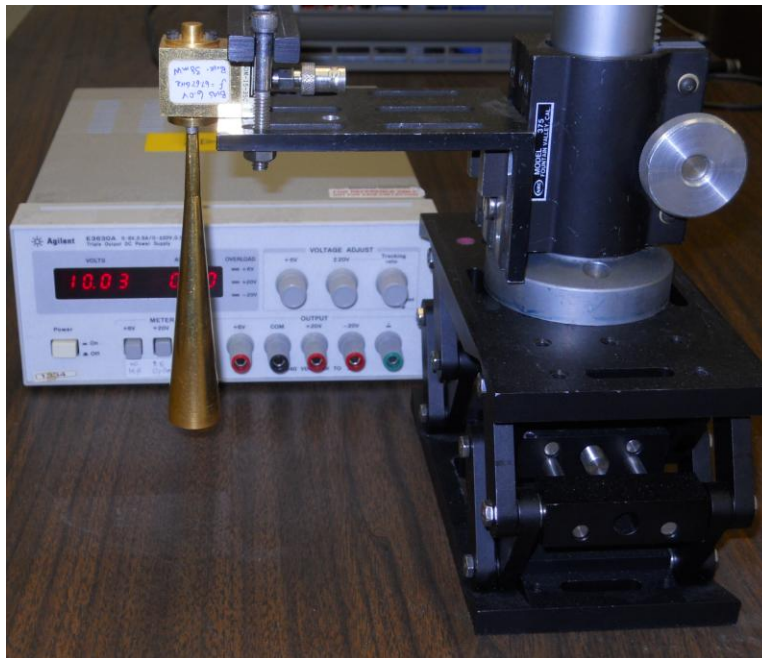*3. Fabrication of the MMW delivery system*

Fig. 5. Photograph of the MMW delivery system.

The fabricated MMW exposure system is based on a commercial 60-GHz source with a built-in power amplifier, providing the power levels between 1 µW and 30 mW (Fig. 5). The narrow-angle far-field horn has been purchased to provide an efficient coupling between the source and the exposed eye with an aberration-free

7

Gaussian distribution of the energy from the horn opening. The selected power supply (E3630A, Agilent) provides a stable switching-transient-free operation of the MMW source. The MMW delivery system is mounted on the Z-axis manipulator to allow precise positioning of the horn opening relative to the eye.

As an alternative to recording from the retina, we next planned to record from visual cortex. We designed and fabricated a flexible parylene-based micro-electrocorticographic (µECoG) array for placement in the V1 cortex to evaluate the possibility of recording evoked visual responses.

During early retinal and cortical placement tests, we compared the arrays with thicknesses ranging from 10 to 40 µm and selected the 30 µm thickness as optimal in terms of mechanical strength and flexibility during surgical handling for array implantation. At the selected Parylene thickness of 30 µm and metal layer thickness of 300 nm, the array is sufficiently transparent to the MMWs to prevent their considerable absorption, thus allowing the MMW penetration into the cortical tissue and avoiding the array heating.

As shown on Figure 6, the array has 32 recording electrodes, with the recording sites having a radius of 150 µm and area of 70,685 µm^2. Spacing between the adjacent sites is 1.9 mm. Perforations are created between the sites in order to promote the array wettability and thus tighter coupling with the cortex. Circumferential ground electrode is designed to provide a wide spatial averaging thus improving the cancellation of electrophysiological noise outside of the array. Integration between the array and a percutaneous zero insertion force (ZIF) connector is implemented with the 10-mm-long monolithic cable on the same wafer. The key wafer processing steps are shown in Figure 7. The three-mask fabrication steps are needed to produce seven µECoG devices on a 4-inch wafer. After microfabrication the arrays were released from the wafer. Two representative arrays are shown in Figure 8.
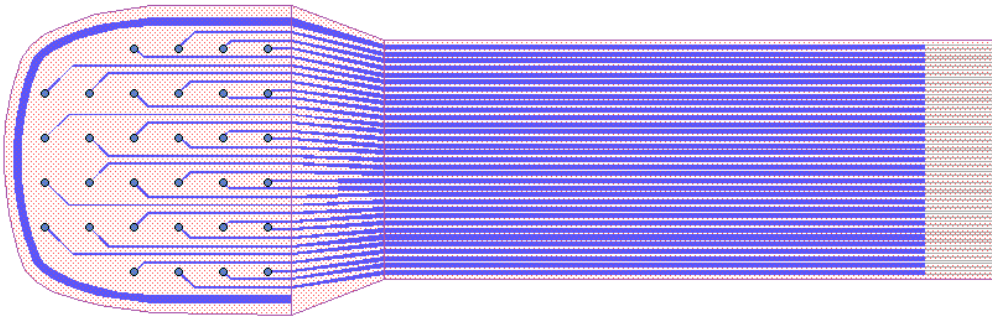

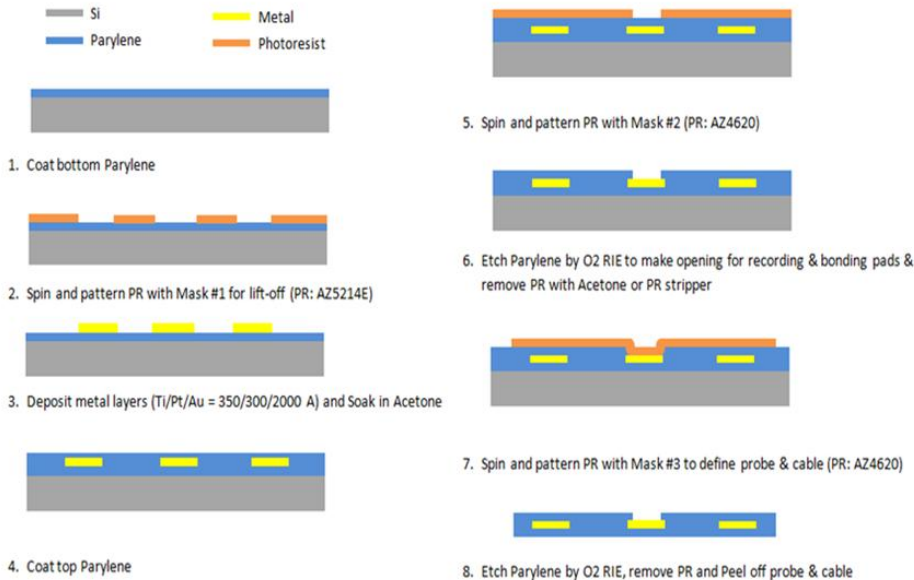Figure 6. Design of the micro-electrocorticographic (µECoG) probe

Figure 7. Process Flow for µECoG microfabrication

Figure 8. Two µECoG arrays released from a silicon carrier wafer.

In conclusion, we have designed and fabricated the µECoG array for placement in the rat V1 cortex for recording evoked visual responses.

Task 2a: Active sensor for mobility aid to blind

RGB-D Camera based SLAM: Accurate disparity maps are a key element in carrying out successful navigation and obstacle avoidance tasks. Most stereo matching algorithms that generate disparity maps are formulated to minimize a pre-defined energy function. Although many advanced stereo matching have been proposed, none of them provide reliable results in textureless environments. Recently, a cost-effective RGB-D sensor developed by Primesense was introduced. It is the reference design for the Microsoft Kinect game interface. The RGB-D camera uses Infra-Red to obtain depth information registered to RGB images, and streams both a depth map and RGB images at 30 FPS. The sensor is shown in Fig. 9. The sensor was used to provide more accurate disparity information of indoor textureless regions in our application. The two main goals of augmentation of the sensor in our application are as follows. First, we aim to have baseline for performance comparison of stereo sensors in textureless Indoor environments. Second, we wish to test the feasibility of a stereo and RGB-D camera hybrid sensor for the navigation tasks.

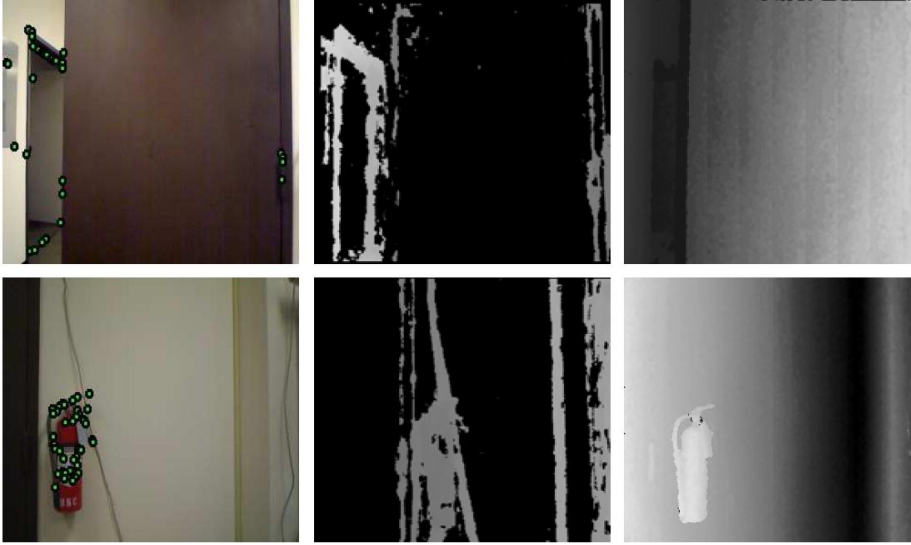Fig. 9. Primesensor, a RGB-D sensor.

9

Fig. 10. Disparity map experiments in low textured areas. Left: RGB camera images. Center: Disparity maps generated by a stereo camera. Right: Disparity maps generated by a RGB-D camera.

As depicted in 10, a stereo camera based system does not provide correct disparity information in low texture scenes as shown in the 2nd column compared to those generated by Primesensor indicated in the 3rd column. As a consequence, a blind subject may receive incorrect feedback information, heading to possible collision. In order to verify the performance of a RGB-D sensor in a guidance system, experiments were conducted for a simple navigation task.

A subject starts from one end of a corridor and aims to reach the other end of the corridor. As shown in 11, the experiment environment has solid walls and reflective floors, which is quite common in indoor environments. Fig. 11 shows that the 3D depth map from the stereo camera is relatively inaccurate and results in inconsistency of the traversability map in the experiment area. From the 2nd column of the 2nd row of the left side of Fig. 11 and on, errors accumulate when building the traversability map of an environment consisting of red and green dots. This spurious information in the map causes the navigation algorithm to fail to find an appropriate way point and a safe path. As described in the 4th column of the left side of Fig. 11, the stereo camera based navigation system hallucinates obstacles that do not exist, and steers a subject in the wrong direction. In the right side of Fig. 11, we replace the stereo system by a RGB-D camera. The dense traversability map is significantly more accurate and consistent with the real corridor environment. It is worth noting that the low textured experiment area still affects the visual odometry performance of the system since we perform visual odometry on RGB images. However, traversability map and navigation worked much more robustly than the navigation system with a stereo camera pair. The performance and reliability of the system improved. In conclusion, RGB-D camera sensor can be a successful alternative of a stereo camera based system when navigating indoors, while a stereo camera based system can still work effectively for outdoor navigation tasks, the sensors effectively complementing each other.

Top row: Gray scale converted RGB image
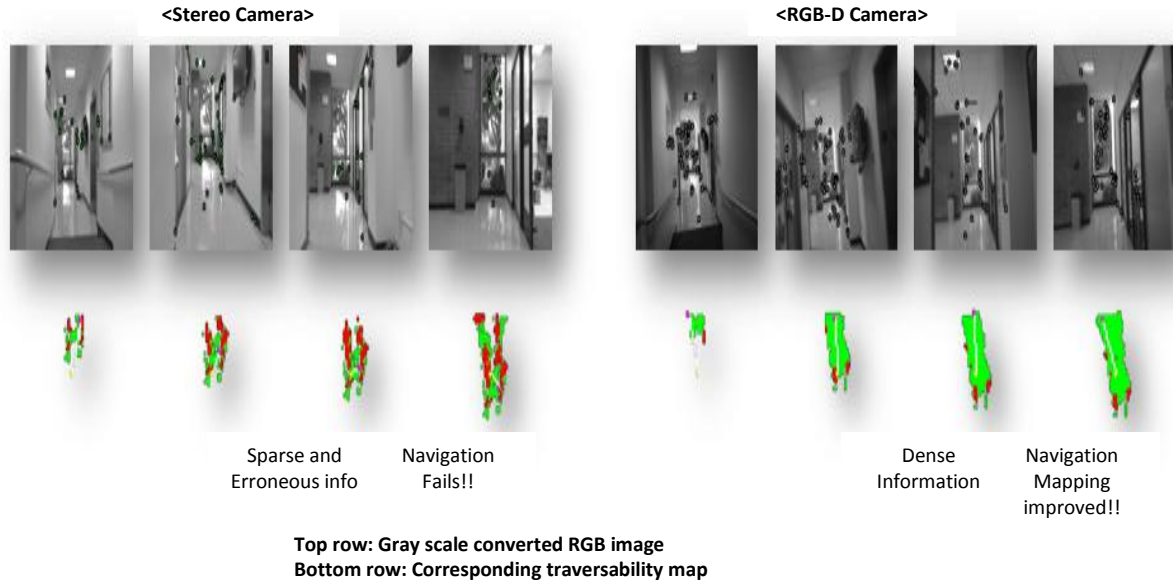Bottom row: Corresponding traversability map

Fig. 11. Four snapshots of traversability map of the system with a pair of stereo camera (left) and with Primesensor (right). More accurate 3D estimation of the indoor environment was achieved by using RGB-D sensor which leads more robust guidance.

New prototype implementation of the wearable RGB-D navigation system connects (Fig 12) to a laptop using USB 2.0 and guarantees real-time streaming (~60 fps) of RGB and depth information without loss, and gives 20~30% speed increase in the entire navigation process compared to stereo camera based system. Also, the new prototype consumes approximately 20% of power compared to the stereo camera prototype meaning much longer life which is crucial for wearable system. In order to verify the performance of an RGB-D sensor in a guidance system, preliminary experiments were conducted for a simple navigation task. RGB-D sensors can be a successful alternative to a stereo camera based system when navigating indoors. One limitation of this sensor is that it only works indoors.

Fig.12 The new prototype - glasses-type RGB-D sensor

Camera motion tracking: We have demonstrated new prototype implementation of the wearable RGB-D navigation system that can create an occupancy grid map of a 3D environment solely from RGB-D camera input at real-time. This algorithm allows route planning of the blind by alerting users about potential obstacles.

However, challenges still exist in the uncertainty in camera position due to jerky camera motions and hardware limitations. The proposed system calculates camera motions based on 2d feature point detection and their corresponding 3d locations of continuous frames. While point features are robust to large motions, the appearance can change drastically under large aspect changes or motion blur. Furthermore, quality of 3d point clouds generated from wearable vision sensors such as a short baseline camera or a short range RGB-D sensor is generally much poorer than what laser sensors provide.

By analyzing performance of the motion tracking algorithm using a RGB-D sensor on the new indoor dataset, we have verified that the system suffers from a lack of the number of reliable 2d feature points and 3d points to estimate camera motion in some cases as shown in Fig.13 and Fig. 14. This is because our system has no constraints in camera position and their viewing direction unlike mobile robot platforms which have a fixed camera position to perceive as abundant information as possible.

Some researchers have proposed to use the adaptive thresholding method in feature tracking to maintain a certain number of features to track. However, lowered threshold provides very weak feature points to track and does not help to improve the tracking performance in our experiments.

Fig. 13. Lack of reliable feature points (green) to track to calculate accurate camera motion. Red bar indicates displacement of the tracked features from the previous frame.
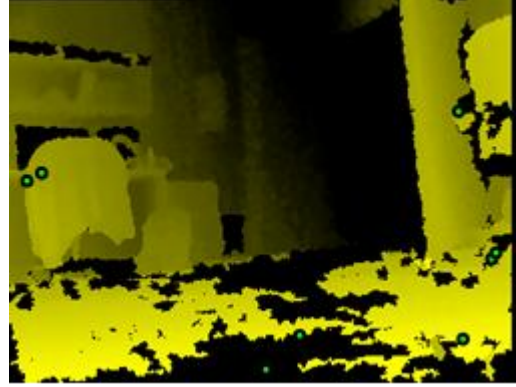

Fig. 14. Depth map of the same scene. The brighter the closer in distance. Black pixels are missing depth information and containing no 3d information.

We first proposed to use both vision sensor and IMU for camera tracking to tackle this problem. Inertia-visual sensor fusion has been proven to provide much more robust tracking results due to complementary characteristics of IMU and camera. An IMU sensor consisting of an accelerometer and a gyroscope is capable of tracking very fast rotation, drifts with time. IMU sensor provides the camera motion tracking algorithm with resilience in rotation estimation in case the visual odometry fails to track camera motion. Quaternion is known to represent rotation in 3D more stable manner than other representations. Rotation calculation using quaternion representation has been implemented in the system.

We are also developing a more robust camera motion tracking algorithm using not only point features but also lines from RGB images. As indicated in Fig. 15 and Fig. 16, Probabilistic Hough transform algorithm detects lines in RGB images. Displacement of extracted lines in an image space is traced using well-known KLT tracker. By validating the homography between two views, falsely matched elements are discarded. This method performs in more stable manner over line matching algorithms that utilize end-point of lines. Additionally, line detection and tracking parts are implemented using both CPU and GPU for speed enhancement.
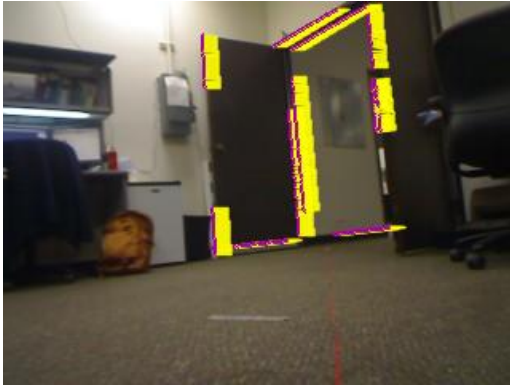

Fig. 15. The same scene of Fig.1 with line extraction (purple) and tracking results (yellow). Line features provide more reliable tracking performance. The camera was rotating to the left.

Fig. 16. Another frame with line extraction (purple) and tracking results (yellow). The camera was moving forward.

Task 2b: An advanced neural interface system for a cortical visual prosthesis

A visual prosthesis that employs multiple arrays of microelectrodes implanted into the primary visual cortex affords the opportunity for restoring useful vision to persons who have become blind due to injuries that render them unsuitable for a retinal level visual prosthesis. However, there is little data on the optimal depth(s) or design for intracortical stimulation electrodes in humans.

Out task is to design a 4-shank, 16-site microstimulating array with integrated cable suitable for animal testing, and validate an expected lifetime of at least 2 years *in vivo* by accelerated soak-testing at 70°C. The ultimate goal is a device with a project lifetime of 20 years *in vivo.*
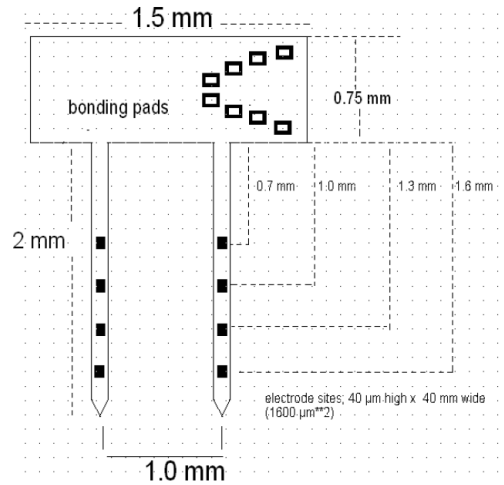

Fig. 17: Schematic of cortical visual prosthetics array based on thick silicon substrate.

Subtask 2b.1.1 Design a 4-shank, 16-site microstimulating array

A preliminary design of the microstimulating probe suitable for implantation into cat cerebral cortex has been completed (Fig. 1717). The array will contain 4 silicon shanks, each with 4 electrode sites. Each shank will be 2 mm in length, to span the full depth of the feline sensory-motor cortex. Unlike the thin "Michigan probes" we will use mechanically-sturdy probe shanks fabricated by DRIE and with a special tip-shaping technique which can penetrate through the pia mater covering the human cerebral cortex. The surface areas of the stimulating sites will be 2,000 μm^2. Each of the electrode sites will be coated with sputtered iridium oxide film (SIROF) to increase their charge injection capacity.

The mask layout design set was completed, and devices have been successfully fabricated at the UCLA Nanofabrication cleanroom facility and were released at HMRI. Details of the device are shown in Figure 18. Half of the devices are monolithically integrated (Figure 18(a)), i.e., the probe shanks supporting the microelectrodes, the flexible cables with their metal interconnect lines, and the bonding area for connection to external components are implemented as one continuous entity. We also have fabricated a version in which the parylene cables terminate in micro-bonding pads rather than at electrode shanks. These cables (Figure 18(b)) can be rivet-bonded to custom silicon-based multi-electrode arrays. This will enable sturdy arrays that can easily penetrate into the brain, but with very flexible parylene cables by which they would be connected to the signal source. Additional wafer processing will be needed for fabrication of the silicon devices.
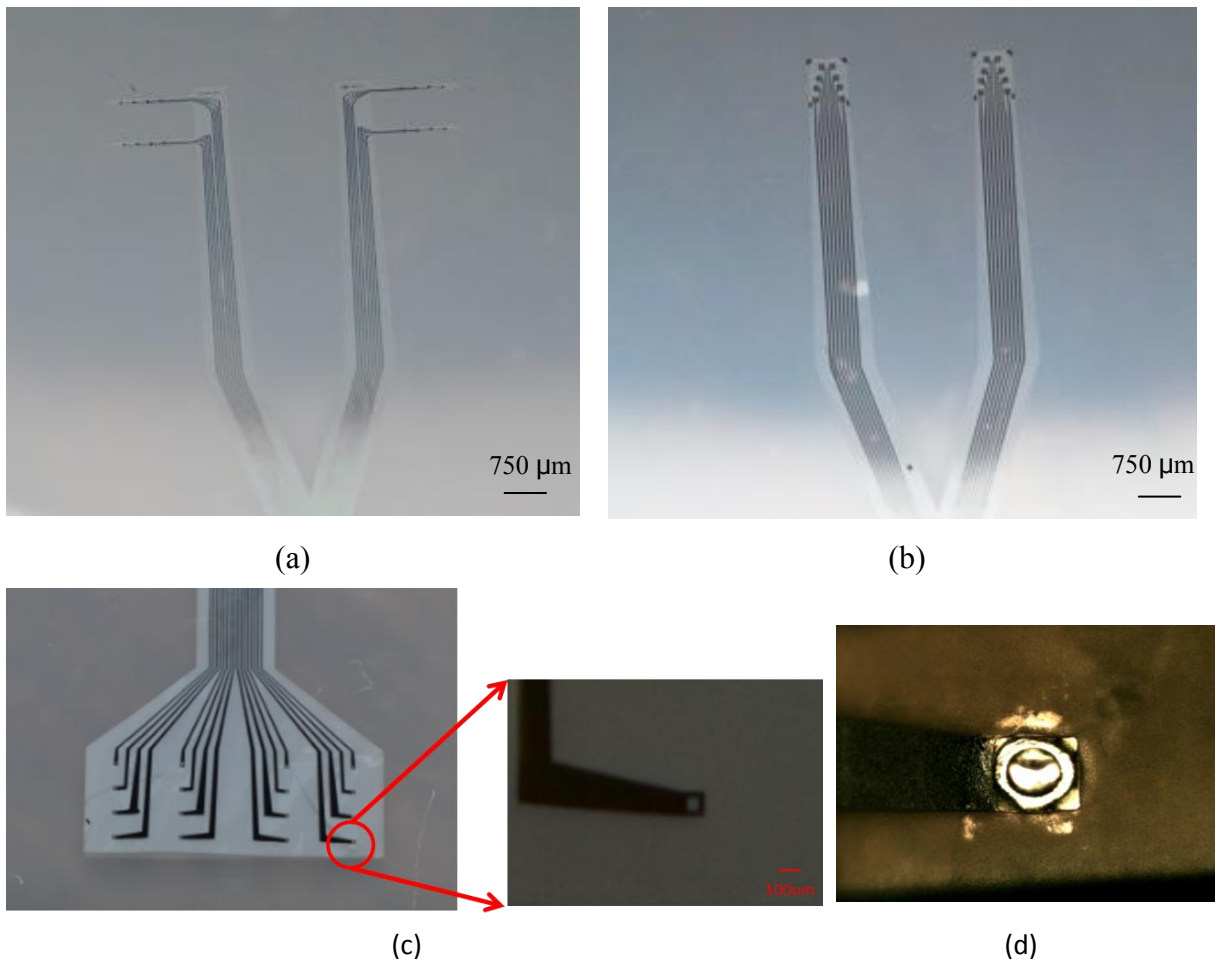
(a)

(b)

(c)

(d)

Figure 18: Images of the visual cortical microelectrode arrays. (a) A monolithic design: Two 2-shank microelectrode arrays which will form a 2 x 2-shank configuration. The device can be a stand-alone array or can be attached to a rigid "backbone" structure of the same shape for greater rigidity. (b) A hybrid approach: The Parylene device will be interfaced with silicon shanks for rigidness and with customized electrode designs. (c) Perforated vias are created on bonding areas to enable rivet-bonding to PCB assembly. (d) Image of rivet-bonded junction. The gold bump forms a tight interface between the top device and the bottom metal pads of the PCB assembly.

Figure 19 shows the Parylene device attached to the printed circuit board (PCB) which contains two Omnetics connectors on its backside (not visible on the photo). The 4 electrode shanks, each with 4 micro-electrode sites, are at the lower right. We will test crosstalk, impedances, charge storage capacity, and charge injection capacity.
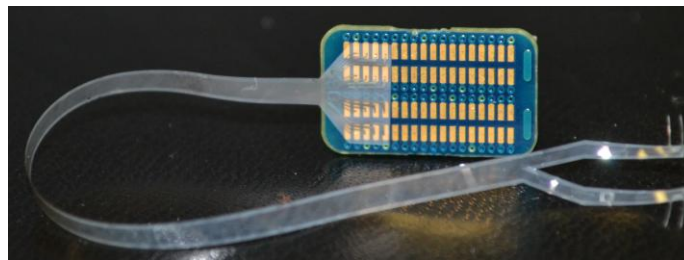

Figure 19: The monolithic Parylene C-based cortical visual prosthesis. Assembly of the fabricated Parylene device with the PCB which contains two Omnetics connectors on its backside (not visible). Rivet bonding was used to interface the Parylene device to the PCB's metal pads. The percutaneous assembly enables testing and implantation.

Subtask 2b.1.2 Develop integrated cable suitable for chronic implantation

We are developing an integrated flexible Parylene cable that will be interfaced to the microelectrode array shown in Fig. 19. The integrated cable is fabricated by batch processing on silicon wafers, and reduces the bulk and stiffness of cables with many conductors. Our approach is to coil the batch-processed integrated cables around a segment of .025-inch diameter silicone tubing, and then overcoat the assembly with a layer of silicone elastomer. This approach will enhance the durability and longevity of the electrical connections, and allow the cable to flex in all directions, unlike a flat cable which cannot flex laterally in the same plane. The cable must be fabricated as a planar (2-dimensional) structure, which then must be coiled into a helical shape in a manner that minimizes stress and also uses the area of the 4-inch wafer most efficiently. So as to optimize yield. We evaluated several design parameters.. This instance (Fig. 20a) showed that a small curvature in the cable in the plane of the wafer would fit the 4-in diameter silicon wafer also could be coiled into a helix wound around a silicone tube (Fig. 20c). However, fabrication considerations would render this design unpractical, since the ends of the cables are too close to the edge of the wafer where edges effects typically occur during fabrication. During the next quarter we will use COMSOL finite element modeling software to optimize wafer utilization and minimize stress during winding,
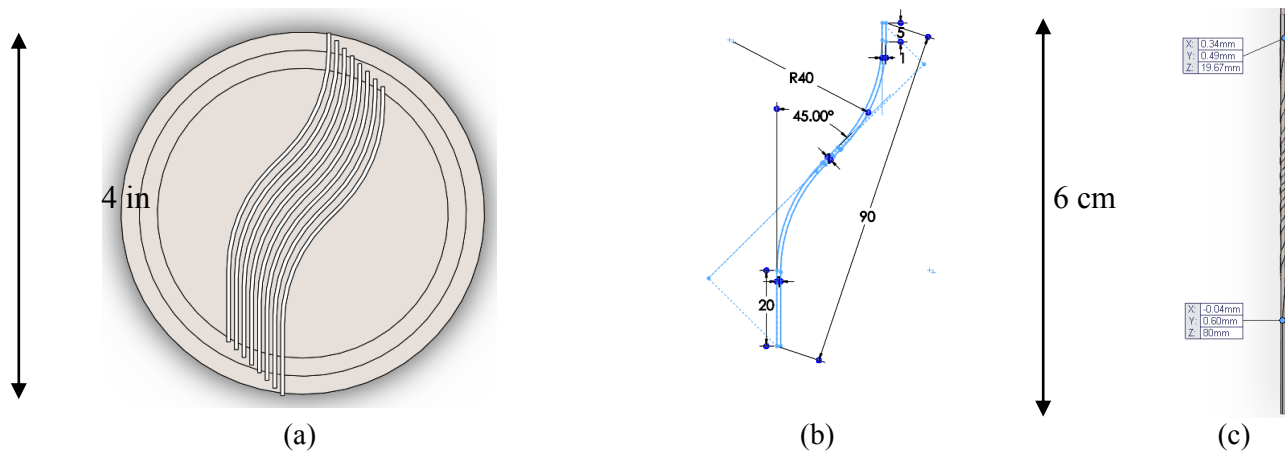

| (a) | (b) | (c) |

Fig. 6: Preliminary designs and simulation of integrated cables: (a) a sample placement of slightly curved cables, placed in 4-in diameter (outer-most) circle, (b) Trial parameters for the planar cable to expediate winding into a helix (c) a view of flexible cable after it is wound around a section of silicone tubing .

We conducted a complete wafer fabrication cycle for the parylene cable, in order to validate all of the process steps. This run was to establish the processing parameters for subsequent runs which will yield usable cables The run encompassed the following operations: 1. Fiducial etching onto the silicon wafer, 2. Coating the wafer with the base Parylene-C layer, 3. deposition of gold electrode sites and conductor traces (Metallization) 4. Deposition of the top Parylene-C layer, 5. Opening of the top layer to expose electrodes sites, and 6. Shaping of the device by etching through the two Parylene C layers. This run will serve as a model for the subsequent rung that will produce cables that can be integrated with the penetrating silicon electrode carrier and attached to a percutaneous connector.

Subtask 2b.1.3 Develop a method of bonding electrode array and the integrated cable

Because of the soft nature of these cable substrates, conventional bonding methods such as wedge or ball bonding will cannot be used to bond the conductors to the silicon electrode arrays. We tested anisotropic adhesives as an alternative to mechanical pressure bonding. Since the flexible cables are not currently available, we purchased and tested commercially available ribbon cables in which the conductors are spaced more widely spaced than in the cable we will eventually use. To make the testbed more realistic (i.e. hard material bonded to soft) we used a Parylene-based substrate (Fig. 21).

The anisotropic adhesive must be approximately 25 µm or thinner when cured to be electrically conductive, which requires application of considerable compressive force without disturbing the alignment between eh points of electrical contact. This was somewhat challenging given the small dimension of the bond pads on the Parylene device (75 µm x 100 µm) Nonetheless, we achieved conductive connections in some of the test samples, and are refining the process.
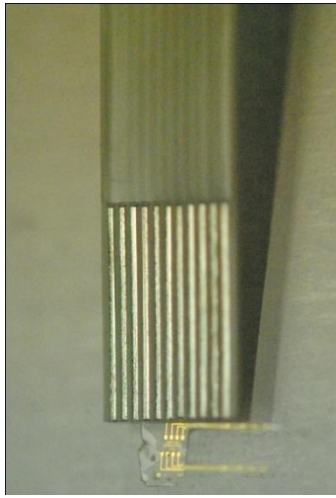
Fig. 7: Test bed for evaluating anisotropic adhesive: The low-density ribbon cable (top) and Parylene-based devices (bottom), before applying the adhesive.

Device Microfabrication

The mask layout design set was completed, and devices have been successfully fabricated at the UCLA Nanofabrication cleanroom facility and were released at HMRI. Details of the device are shown in Figure 1. Half of the devices are monolithically integrated (Figure 22(a)), i.e., the probe shanks supporting the microelectrodes, the flexible cables with their metal interconnect lines, and the bonding area for connection to external components are implemented as one continuous entity. We also have fabricated a version in which the parylene cables terminate in micro-bonding pads rather than at electrode shanks. These cables (Figure 22(b)) can be rivet-bonded to custom silicon-based multi-electrode arrays. This will enable sturdy arrays that can easily penetrate into the brain, but with very flexible parylene cables by which they would be connected to the signal source. Additional wafer processing will be needed for fabrication of the silicon devices. Figure 23 shows the Parylene device attached to the printed circuit board (PCB) which contains two Omnetics connectors on its backside (not visible on the photo). The 4 electrode shanks, each with 4 micro-electrode sites, are at the lower right.
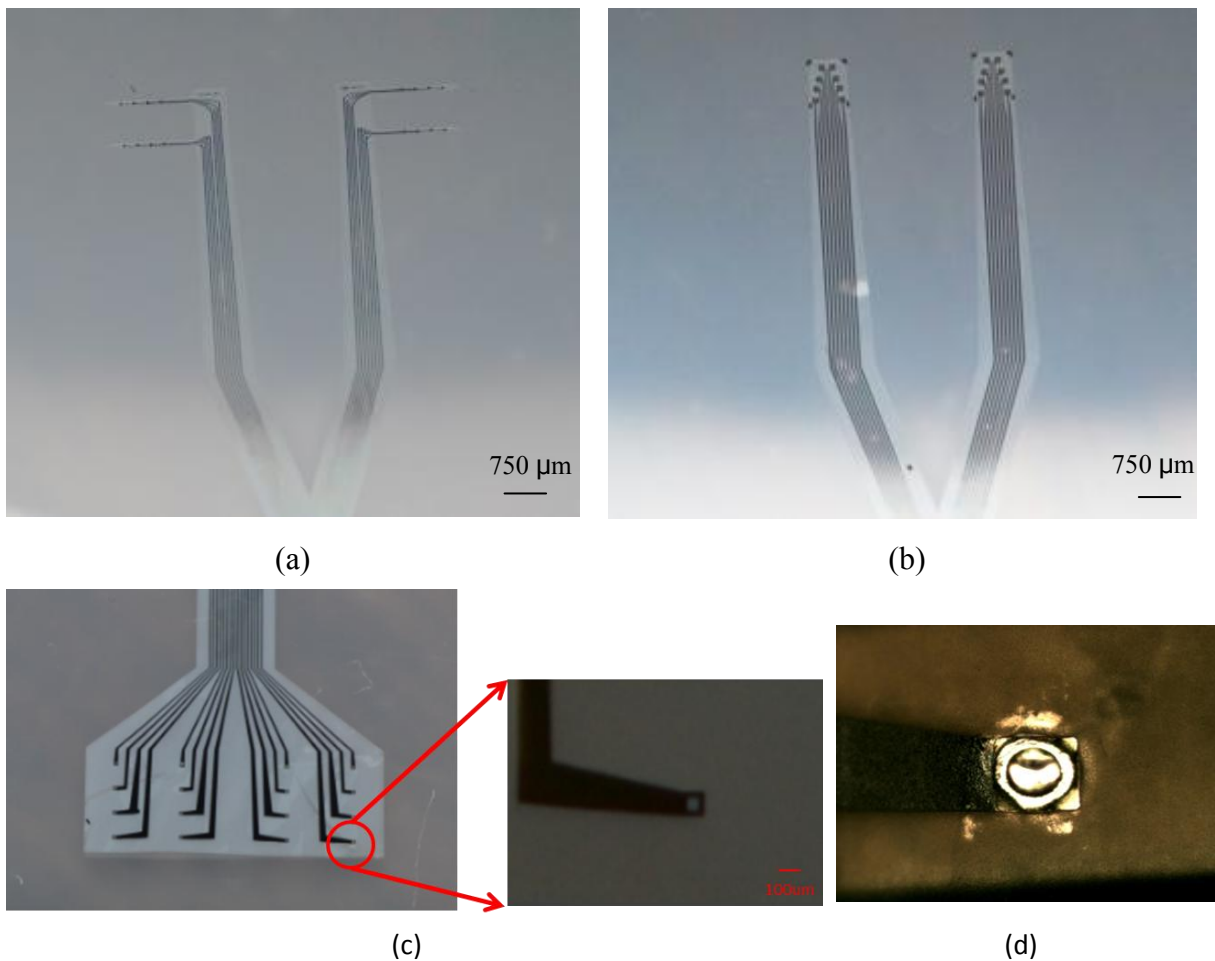
Figure 22: Images of the visual cortical microelectrode arrays. (a) A monolithic design: Two 2-shank microelectrode arrays which will form a 2 x 2-shank configuration. The device can be a stand-alone array or can be attached to a rigid "backbone" structure of the same shape for greater rigidity. (b) A hybrid approach: The Parylene device will be interfaced with silicon shanks for rigidness and with customized electrode designs. (c) Perforated vias are created on bonding areas to enable rivet-bonding to PCB assembly. (d) Image of rivet-bonded junction. The gold bump forms a tight interface between the top device and the bottom metal pads of the PCB assembly.
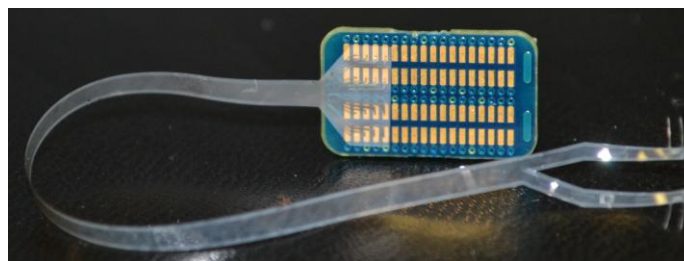

Figure 23: The monolithic Parylene C-based cortical visual prosthesis. Assembly of the fabricated Parylene device with the PCB which contains two Omnetics connectors on its backside (not visible). Rivet bonding was used to interface the Parylene device to the PCB's metal pads. The percutaneous assembly enables testing and implantation.

KEY RESEARCH ACCOMPLISHMENTS

- Demonstrated NIR-OCT as a means of detect blood oxygenation
- Development of real-time user-friendly software interface for measuring evoked retinal responses;

- Measurement of evoked retinal responses epiretinally, subretinally, and in the visual cortex of the rat using custom-fabricated flexible multi-electrode arrays;
- Fabrication of the MMW delivery system.
- Fabrication of custom arrays for visual cortex based prosthesis
- **Data collection of RGB-D camera and IMU**: New indoor datasets (PHE101 at USC) for the camera motion estimation with ground truth have been collected to quantitatively analyze the performance of the camera motion estimation algorithm on different H/W configurations (stereo camera, IMU+stereo camera, Primesensor, and Primesensor+IMU)
- **Representation of rotation using quaternions**: Quaternions are known to represent rotation in 3D in a more stable manner than other representations. The Rotation calculation using quaternion representation has been implemented in the system.
- **Robust motion estimation using various geometric primitives**: We are also developing a more robust camera motion tracking algorithm using not only 2D point features but also lines from RGB images. The displacement of extracted lines in an image space is estimated using the well-known KLT tracker. By validating the homography between two views, falsely matched elements can be discarded. This method performs in more stable manner over line matching algorithms that utilize end-point of lines. Additionally, line detection and tracking parts are implemented using both CPU and GPU for speed enhancement.

REPORTABLE OUTCOMES

Journal article

- X. Y. Zhang, J. Hu, R. W. Knighton, X-R Huang, C. A. Puliafito, and S. Jiao, "Dual-band spectral-domain optical coherence tomography for *in vivo* imaging the spectral contrasts of the retinal nerve fiber layer", Optics Express **19**, 19653-19659 (2011).
- Y. Lee et al. *Best Research Demo Award*, 2nd Annual Ming Hsieh Department of Electrical Engineering Research Festival, USC
- Y. Lee and G. Medioni, RGB-D camera Based Navigation for the Visually Impaired, RSS 2011 RGB-D: Advanced Reasoning with Depth Camera Workshop, June 2011, pp. 1 – 6.

CONCLUSION

In conclusion, we have conducted a number of research projects that relate to issues facing warfighters who experience ocular trauma. This research can potentially lead to better methods of diagnosis and treatment. The OCT work advances ocular imaging for better diagnoses of issues related to blast trauma (such as retinal detachment). The millimeter wave stimulation, active sensor for navigation aid, and electrode for visual cortex prosthesis all represent potential methods for treatment of blindness or low-vision.

APPENDICES

Dual-band spectral-domain optical coherence tomography for *in vivo* imaging the spectral contrasts of the retinal nerve fiber layer

Xiangyang Zhang,[1] Jianming Hu,[1,3] Robert W. Knighton,[2] Xiang-Run Huang,[2] Carmen A. Puliafito,[1] and Shuliang Jiao[1,*]

[1]*Department of Ophthalmology, Keck School of Medicine, University of Southern California, Los Angeles, CA 90033, USA*
[2]*Bascom Palmer Eye Institute, University of Miami Miller School of Medicine, Miami, FL 33136, USA*
[3]*Chongqing Key Laboratory of Optics and Engineering, Chongqing Normal University, Chongqing 40047, China*
*[*]sjiao@usc.edu

Abstract: The ultimate goal of the study is to provide an imaging tool to detect the earliest signs of glaucoma before clinically visible damage occurs to the retinal nerve fiber layer (RNFL). Studies have shown that the optical reflectance of the damaged RNFL at short wavelength (<560nm) is reduced much more than that at long wavelength, which provides spectral contrast for imaging the earliest damage to the RNFL. To image the spectral contrast we built a dual-band spectral-domain optical coherence tomography (SD-OCT) centered at 808nm (NIR) and 415nm (VIS). The light at the two bands was provided by the fundamental and frequency-doubled outputs of a broadband Ti:Sapphire laser. The depth resolution of the NIR and VIS OCT systems are 4.7μm and 12.2μm in the air, respectively. The system was applied to imaging the rat retina *in vivo*. Significantly different appearances between the OCT cross sectional images at the two bands were observed. The ratio of the light reflected from the RNFL over that reflected from the entire retina at the two bands were quantitatively compared. The experimental results showed that the dual-band OCT system is feasible for imaging the spectral contrasts of the RNFL.

References and links

1. H. A. Quigley, "Glaucoma," Lancet 377(9774), 1367–1377 (2011).
2. L. A. Kerrigan-Baumrind, H. A. Quigley, M. E. Pease, D. F. Kerrigan, and R. S. Mitchell, "Number of ganglion cells in glaucoma eyes compared with threshold visual field tests in the same persons," Invest. Ophthalmol. Vis. Sci. 41(3), 741–748 (2000).
3. M. L. Gabriele, G. Wollstein, H. Ishikawa, L. Kagemann, J. Xu, L. S. Folio, and J. S. Schuman, "Optical coherence tomography: history, current status, and laboratory work," Invest. Ophthalmol. Vis. Sci. 52(5), 2425–2436 (2011).
4. H. G. Lemij and N. J. Reus, "New developments in scanning laser polarimetry for glaucoma," Curr. Opin. Ophthalmol. 19(2), 136–140 (2008).
5. R. W. Knighton, X. Huang, and Q. Zhou, "Microtubule contribution to the reflectance of the retinal nerve fiber layer," Invest. Ophthalmol. Vis. Sci. 39(1), 189–193 (1998).
6. X.-R. Huang and R. W. Knighton, "Microtubules contribute to the birefringence of the retinal nerve fiber layer," Invest. Ophthalmol. Vis. Sci. 46(12), 4588–4593 (2005).
7. B. Fortune, L. Wang, G. Cull, and G. A. Cioffi, "Intravitreal colchicine causes decreased RNFL birefringence without altering RNFL thickness," Invest. Ophthalmol. Vis. Sci. 49(1), 255–261 (2008).
8. G. M. Pocock, R. G. Aranibar, N. J. Kemp, C. S. Specht, M. K. Markey, and H. G. Rylander 3rd, "The relationship between retinal ganglion cell axon constituents and retinal nerve fiber layer birefringence in the primate," Invest. Ophthalmol. Vis. Sci. 50(11), 5238–5246 (2009).
9. X.-R. Huang and R. W. Knighton, "Altered F-actin distribution in retinal nerve fiber layer of a rat model of glaucoma," Exp. Eye Res. 88(6), 1107–1114 (2009).

10. X.-R. Huang, W. Kong, Y. Zhou, and G. Gregori, "Distortion of axonal cytoskeleton: an early sign of glaucomatous damage," Invest. Ophthalmol. Vis. Sci. **52**(6), 2879–2888 (2011).
11. X.-R. Huang, Y. Zhou, W. Kong, and R. W. Knighton, "Reflectance decrease prior to thickness change of the retinal nerve fiber layer in glaucomatous retinas", Invest. Ophthalmol. Vis. Sci., published ahead of print July 5, 2011.
12. R. W. Knighton and X.-R. Huang, "Directional and spectral reflectance of the rat retinal nerve fiber layer," Invest. Ophthalmol. Vis. Sci. **40**(3), 639–647 (1999).
13. X.-R. Huang, Y. Zhou, W. Kong, and R. W. Knighton, "Change of retinal nerve fiber layer reflectance correlated with cytostructural change in glaucoma," ARVO Meeting Abstracts (Fort Lauderdale, Florida 2011), 52:2442.
14. M. Ruggeri, G. Tsechpenakis, S. Jiao, M. E. Jockovich, C. Cebulla, E. Hernandez, T. G. Murray, and C. A. Puliafito, "Retinal tumor imaging and volume quantification in mouse model using spectral-domain optical coherence tomography," Opt. Express **17**(5), 4074–4083 (2009).
15. X. Zhang, H. F. Zhang, C. A. Puliafito, and S. Jiao, "Simultaneous in vivo imaging of melanin and lipofuscin in the retina with photoacoustic ophthalmoscopy and autofluorescence imaging," J. Biomed. Opt. **16**(8), 080504 (2011).
16. R. W. Knighton and X.-R. Huang, "Visible and near-infrared imaging of the nerve fiber layer of the isolated rat retina," J. Glaucoma **8**(1), 31–37 (1999).
17. Scott Prahl, "Optical Absorption of Hemoglobin," *http://omlc.ogi.edu/spectra/hemoglobin/summary.html*.

1. Introduction

Glaucoma, one of the leading causes of irreversible blindness worldwide, occurs when the retinal ganglion cells and their axons in the retinal nerve fiber layer (RNFL) and optic nerve degenerate in a characteristic and identifiable pattern called glaucomatous optic neuropathy (recently reviewed in Ref. 1). Untreated glaucoma may lead to permanent loss of vision, which motivates attempts to detect the earliest signs of the disease. Early diagnosis will permit early medical intervention to prevent vision loss. Current clinical methods for glaucoma diagnosis detect degenerative damage after it has already occurred, either structural damage (tissue loss in the optic disc, RNFL or macula) or functional damage (loss of visual sensitivity). Some data suggest that structural damage can occur many years before detectable loss of visual sensitivity [2] and a variety of optical approaches to structural assessment have been pursued. In particular, recent advances in optical coherence tomography (OCT) for glaucoma diagnosis have mostly focused on structural measurements [3].

In the case of the RNFL, some clinical and laboratory methods have progressed beyond the measurement of structure to the assessment of the optical properties of the tissue. For example, the commercially available technology of scanning laser polarimetry uses retardation by RNFL birefringence as a measure of RNFL integrity [4]. The optical properties of the RNFL depend on axonal structure at the submicroscopic level; its birefringence, for example, arises from parallel intracellular fibrils called microtubules [5–8]. Importantly, studies of the RNFL in a rat model of glaucoma show that the axonal cytoskeleton can change before the decrease in RNFL thickness [9,10] and in pilot studies we used high resolution small animal OCT operating at a center wavelength of 830 nm to confirm that there was no decrease in the RNFL thickness measured *in vivo* for the same rats (data unpublished). Even more promising, RNFL reflectance can decline before histologically detectable change in the axonal cytoskeleton [11]. Thus, the measurement of RNFL optical properties may allow a means to detect changes in cellular substructure that occur before axonal degeneration. This in turn could lead to diagnostic methods that reveal a therapeutic window during which permanent damage might be prevented.

The RNFL reflectance at all wavelengths arises from light scattering by cylindrical structures, with RNFL reflectance spectra suggesting the presence of at least two scattering mechanisms [12]. The spectra can be fit by a model where the reflectance at wavelengths shorter than 570 nm comes from cylinders with diameters much smaller than the wavelength, but the reflectance at wavelengths longer than ~680 nm comes from cylinders with effective diameters of 350 nm to 900 nm. A recent report showed that the RNFL reflectance in the rat glaucoma model also demonstrated spectral changes; at short wavelengths (< 560nm) the reflectance of the affected RNFL decreased much more than at long wavelengths [13]. This result suggests that the subtle structural alteration of axons in early glaucoma produces a wavelength dependent change in the RNFL reflectance.

In conventional ophthalmic OCT, the RNFL appears as a brightly reflecting layer. Because the light sources used in ophthalmic OCT systems are in the near infrared (NIR), the detected light from the RNFL should come mainly from scattering by thick cylindrical structures, making NIR OCT intrinsically insensitive to the very early changes seen in the rat model of glaucoma. If we shift the wavelength of the OCT to the visible (shorter than 570 nm), however, the changes to the thin cylindrical structures may be detectable. Ideally, an OCT system that covers both long and short wavelengths should be able to image contributions from both the thin and thick cylindrical structures in the nerve fibers. To test this hypothesis, an OCT system working in the visible spectrum (preferably at a center wavelength < 500 nm) is needed.

In this paper we report on our first effort in building and testing an OCT system working at a center wavelength of ~415 nm specifically for imaging the spectral contrast of the RNFL. The current study is a technical preparation for investigations on early diagnosis and progressive assessment of glaucoma using imaging technologies.

2. Experimental system

Figure 1 shows a schematic of the experimental system. The system consists of two spectral-domain OCT systems: one working in the NIR band and the other one working in the visible (VIS) band. A broadband Ti: Sapphire laser (MICRA, center wavelength: 800 nm, bandwidth: 120 nm, Coherent Inc, USA) was used as the fundamental light source. A frequency doubling crystal (BBO, Castech, Fujian, China) was used to convert the laser light to the visible. To ensure a broadband output from the crystal the fundamental laser light was focused into the crystal by a lens of f=14 mm (L1). The light exiting the BBO crystal was first collimated with an achromatic lens of f=40 mm (L2) and then reflected by a long-pass filter (FEL0700, Thorlabs, USA) to separate the visible light from the residual fundamental light.
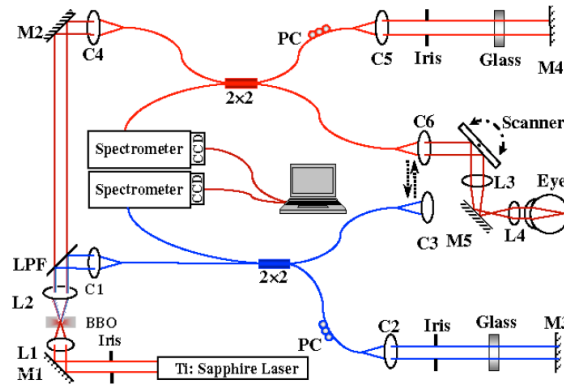

Fig. 1. Schematic of the dual-band OCT system. M1~M5: mirror; L1~L4: lens; BBO: BBO crystal; LPF: long-pass filter. C1~C6: Collimator; PC: Polarization Controller.

The visible light was then coupled into the source arm of a single mode optical fiber-based Michelson interferometer. In the detection arm the reflected light from the sample and reference arms was collimated and detected by a spectrometer, which consisted of an 1800 line/mm transmission grating, a multi-element imaging lens (f=150 mm), and a line scan CCD camera (Aviiva-SM2-CL-2010, 2048 pixels with 10 micron pixel size operating in 12-bit mode, e2V). An image acquisition board (NI IMAQ PCI 1428) acquired the image captured by the camera and transferred it to a workstation (HP xw4600, 4 GB memory) for signal processing and image display. The design of the NIR-OCT is similar to that in our previous publications [14,15] except that the residual fundamental light after the long-pass filter was used as the light source.

After exiting their corresponding optical fibers in the sample arms the visible and NIR probing light beams were collimated with collimators that can be interchangeably connected with the scanning and optical delivery system. The scanning and optical delivery system was built on a modified slit lamp. The probing light beams were scanned by an X-Y galvanometer scanner and delivered to the eye through an achromatic relay lens (f = 75 mm) and an objective lens (f = 19 mm).

3. Results and discussion

3.1 Spectral reflectance of the RNFL

We measured the spectral reflectance of the RNFL of living *ex vivo* rat retinas by using imaging micro-reflectometry (IMR) [13,16]. The result of measurement is shown in Fig. 2. Rectangular areas are defined both on a nerve fiber bundle (black boxes) and nearby gaps (white boxes), where no nerve fiber bundles exist. The average reflected light intensity of both bundle (I_b) and gap (I_g) areas are calculated. Reflectance from RNFL only is then derived as $I = I_b - I_g$. Figure 2B shows the RNFL spectral reflectance of a glaucomatous eye and its control eye in a rat glaucoma model produced by laser treatment of the trabecular meshwork [9–11]. Intra-ocular pressure (IOP) before treatment for both eyes was 24 mmHg. The treated eye was exposed to high IOP for 18 days with peak IOP of 48 mmHg. The spectra were measured 4 weeks after the start of treatment. The experiments showed that glaucoma causes decreased RNFL reflectance at short wavelengths while it remained approximately the same at longer wavelengths.
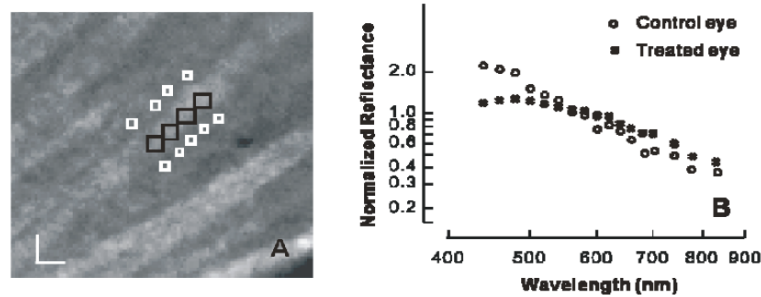

Fig. 2. Measurement of RNFL reflectance. A: typical reflection image of the RNFL; nerve fiber bundles appear as bright stripes; B: calculated spectral reflectance of the RNFL; Bar: 20 μm.

3.2 VIS-OCT experiments

Figure 3 shows the measured spectra and the point-spread functions of the two OCT systems. The center wavelength and full width at half maximum (FWHM) of the NIR light are 808 nm and about 105 nm, respectively. The NIR-OCT achieved a depth resolution of about 4.7 μm and an imaging depth of 2.5 mm in the air. The center wavelength and FWHM of the visible light are 415 nm and 7 nm, respectively. The VIS-OCT achieved a depth resolution of about 12.2 μm and an imaging depth of 1.3 mm in the air.

The system was applied to imaging the normal rat retina *in vivo*. The animals (Sprague Dawley rats, body weight: 600~750 g, Charles Rivers) were anesthetized by intraperitoneal injection of a cocktail containing ketamine (54 mg/kg body weight) and xylazine (6 mg/kg body weight). In the meantime, the pupils were dilated with 10% phenylephrine solution. Drops of artificial tears were applied to the eyes every two minutes to prevent dehydration of the cornea and cataract formation. After anesthetization, the animals were restrained in a mounting tube, which was fixed on a five-axis platform. Raster scans with the fast axis along the horizontal direction were performed. All experiments were performed in compliance with the guidelines of the University of Southern California's Institutional Animal Care and Use Committee.
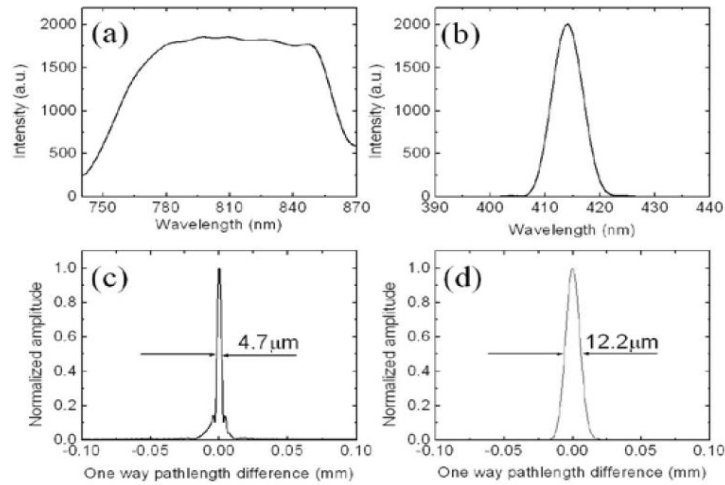
Fig. 3. Measured parameters of the NIR and VIS OCT systems. (a) and (b): spectra of the NIR and VIS OCT systems; (c) and (d): PSF of the NIR and VIS OCT systems.

In the experiment, we collected the NIR and VIS-OCT images sequentially. The initial alignment including finding the area of interest was done with the NIR OCT. After the acquisition of the NIR OCT image we mechanically switched the VIS OCT into position and acquired the VIS OCT images. In our current study the laser energy after the objective lens was measured to be 450 μw for the visible and 750 μw for the NIR light, which are both below the ANSI safety limits for eye imaging. Since the OCT images of the two different bands were not acquired simultaneously they are not completely registered due to movement of the animal during the switching process. The advantage of using the NIR-OCT for alignment is to reduce the retinal exposure to the visible light. The higher axial resolution and greater imaging depth of the NIR-OCT also aided the alignment.
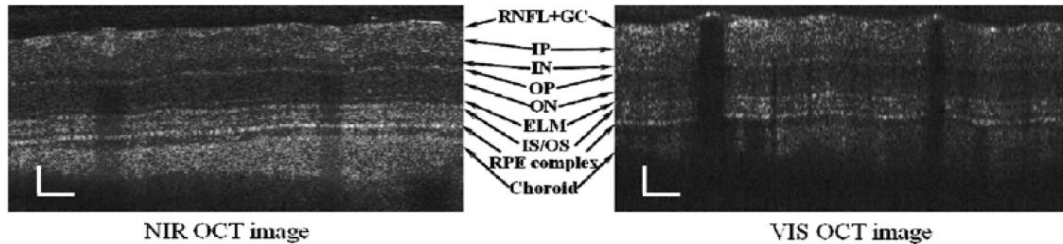

Fig. 4. Sample images of a rat retina acquired with the NIR OCT and VIS OCT. Images consist of 2048 A-lines. Bar: 100 μm.

Figure 4 shows one pair of the acquired NIR and VIS OCT images. The images consist of 2048 A-scans and cover a length of about 1.3 mm across the retina. The differences between the NIR and VIS OCT images are significant. As expected the blood vessels blocked the VIS probing light completely with only reflections from their front boundaries, while the NIR-OCT still revealed some features beneath the vessels. This difference comes from the significant difference of the absorption coefficients of hemoglobin at the two bands: at 415 nm μ_a = 2801.52 (cm^{-1}) for oxy-hemoglobin (HbO$_2$) and μ_a = 1891.79 (cm^{-1}) for deoxy-hemoglobin (Hb); at 808 nm μ_a = 4.58 (cm^{-1}) for HbO2 and μ_a = 3.88 (cm^{-1}) for Hb [17].
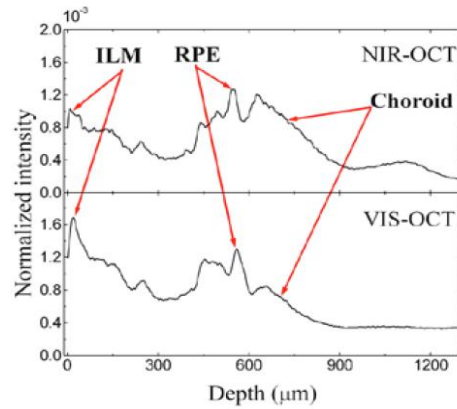
Fig. 5. Normalized average of the A-lines of the OCT images in Fig. 4.

In the NIR OCT image there are strong signals from deep into the choroid. In the VIS OCT image, although we can still recognize all the retinal layers there are much weaker signals from behind the RPE layer due to the higher attenuation coefficient of the RPE in the VIS band. To further demonstrate the different characteristics of the OCT signal in the two bands we averaged all the A-lines of the images in Fig. 4. Before averaging we flattened each image by first drawing their ILMs and then shifting each A-line in the depth direction accordingly. The averaged A-lines are shown in Fig. 5. From Fig. 4 and Fig. 5 we can see that the RPE signal is the strongest in the NIR OCT image. In contrast, the RNFL signal is the strongest in the VIS OCT image. Another noticeable feature is that the boundaries among the different retinal layers in the VIS OCT image are not as clear as those in the NIR OCT image. This feature may be caused by the different depth resolutions of the two OCT systems. Other factors like the differences of the optical properties, e.g. index of refraction of the different layers in the VIS and NIR bands may also play a role.
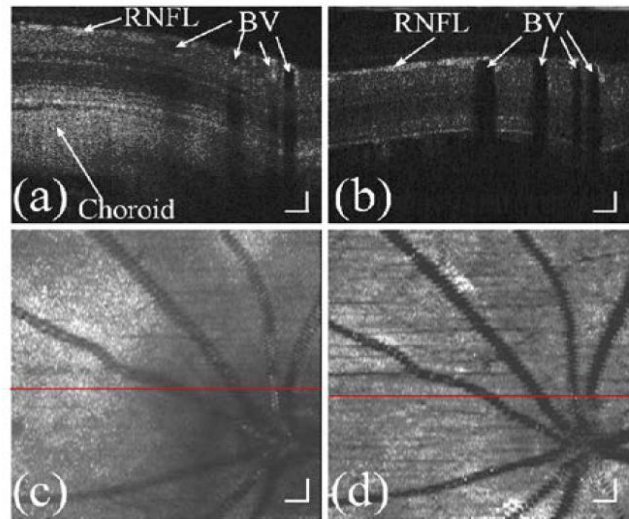

Fig. 6. Retinal images acquired with the NIR and VIS OCT systems. (a): B-scan image of the NIR OCT; (b): B-scan image of the VIS OCT; (c): NIR-OCT fundus image; (d): VIS-OCT fundus image. BV: blood vessel. Bar: 100 μm.

Figure 6 shows another typical pair of NIR and VIS OCT images from an acquired 3D data set, which consists of 512×128 A-scans. Also shown in the figure are the corresponding OCT fundus images, on which the locations of the OCT cross sectional images are marked. We can see that the contrast of the retinal blood vessels is higher in the VIS-OCT fundus

24

image due to the higher attenuation coefficient of the red blood cells in the VIS band. We can also see from the fundus images that the lateral resolution in the VIS band is better since we can recognize some small blood vessels that are not available in the NIR fundus image.

Owing to the depth resolving capability of OCT we can calculate the light reflection from a certain layer of the retina by summation of the OCT signals inside the layer:

$$I_{r(z_1 \sim z_2)}(x) = \sum_{z_1}^{z_2} I_{OCT}(x, z) \tag{1}$$

where I_{OCT} is the OCT intensity signal, x is the coordinates of the horizontal direction, z is the coordinates of the depth, z_1 and z_2 are the lower and upper boundaries of the layer. To calculate the reflections from the RNFL we first segmented the RNFL manually and calculated the reflection from inside the layer. We then calculated the ratio of the RNFL reflection over the fundus reflection calculated from the whole imageing depth using:

$$R_{RNFL} = \frac{I_{r(z_1 \sim z_2)}(x)}{I_{r(total)}}. \tag{2}$$

Figure 7 shows the segmentation of the RNFL boundaries in a pair of NIR and VIS OCT B-Scan images at the same location of the retina. Also shown in the figure are the calculated RNFL reflection ratios. From the calculation we can see that the reflection from the RNFL in the NIR band takes about 5% of the total fundus reflection. In the VIS band, however, the ratio increases to about 10%. The calculation shows that a higher portion of the fundus reflection comes from the RNFL reflection when imaged in the VIS band.
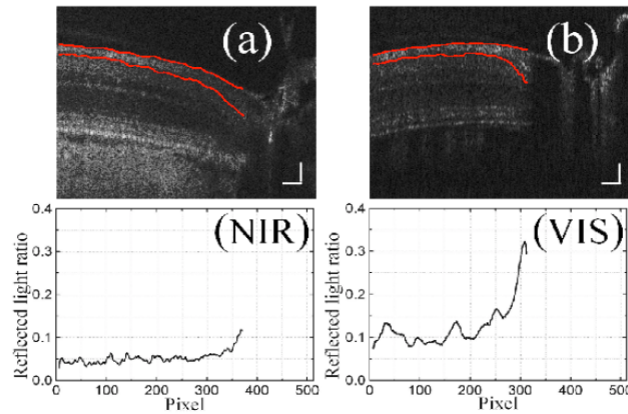

Fig. 7. Calculation of the ratio of RNFL reflection over the total fundus reflection for NIR (a) and VIS (b) OCT B-scans. Bar: 100 µm.

4. Conclusion

We have for the first time built a dual-band OCT system with one band centered at 415 nm and the other at 808 nm for imaging the spectral contrast of the RNFL. The system was successfully applied to imaging the rat retina *in vivo*. Significantly different appearances between the OCT cross sectional images at the two bands were revealed in the preliminary imaging tests. The experiments showed that a higher portion of the fundus reflection comes from the RNFL reflection when imaged in the VIS band. We can conclude that the dual-band OCT system is feasible for imaging the spectral contrast of the RNFL.